THE JOURNAL OF PHYSICAL CHEMISTRY C

Article

pubs.acs.org/JPCC

In Situ Spectroscopic Evidence for Ordered Core−Ultrathin Shell Pt_1Co_1 Nanoparticles with Enhanced Activity and Stability as Oxygen Reduction Electrocatalysts

Qingying Jia,[†] Keegan Caldwell,[‡] David E. Ramaker,[‡] Joseph M. Ziegelbauer,[§] Zhongyi Liu,[§] Zhiqiang Yu,[§] Matthew Trahan,[†] and Sanjeev Mukerjee*[,†]

[†]Department of Chemistry and Chemical Biology, Northeastern University, Boston, Massachusetts 02115, United States

[‡]Department of Chemistry, George Washington University, Washington, D.C. 20052, United States

[§]Electrochemical Energy Research Lab, General Motors Central Research and Development, Warren, Michigan 48090, United States

Supporting Information

ABSTRACT: To truly understand the origin of the enhanced oxygen reduction reaction (ORR) activity of Pt-based electrocatalysts over pure Pt, it is essential to characterize the electrocatalysts under ORR operating conditions. Herein, we report a dealloyed Pt_1Co_1 NP catalyst with Pt mass activity ∼4 times higher than that of Pt/C and with superior stability in proton exchange membrane fuel cells (PEMFCs). Advanced microscopy and *in situ* spectroscopy are combined to show that this electrocatalyst possesses a unique ordered PtCo core−ultrathin with nonporous Pt shell structure, and the structure maintains the desired compositional profiles in the near-surface region even during the ORR in acid. *Ab initio* FEFF8 calculations based on experimentally derived structures reveal that the catalytic enhancements result from cooperative compressive-strain and ligand effects induced by the Co enrichment in the compact core and near subsurface.

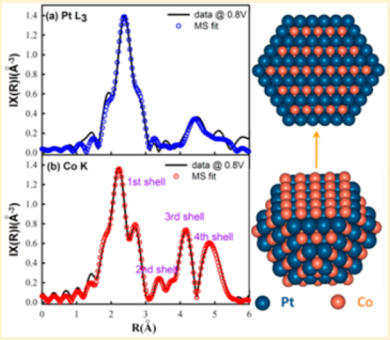

INTRODUCTION

The commercialization of proton exchange membrane fuel cells (PEMFCs) is hindered by the high Pt loading required in the cathode to catalyze the slugguish oxygen reduction reaction (ORR). Pt-based bimetallics have gained considerable attention as they generally display improved ORR activity and stability compared to pure Pt.[1−7] Further, significant progress has been made in understanding the reasons for the increased ORR activity. Previous studies[1,8−12] have demonstrated the crucial role played by subsurface M atoms (M = 3d transition metal) in downshifting the Pt surface d-band center that in turn weakens the Pt−O bond strength. This Pt−O bond weakening enhances the ORR rate by decreasing overpotential for the electro-reduction of OH* (adsorbed hydroxyl intermediate) to H_2O.[13] The model structure single-crystal (SC) $Pt_3Ni(111)$ with a Ni-enriched subsurface has been reported a 10-fold improvement in specific activity over Pt(111)[9] and is the most active Pt−M bimetallic identified. Translation of such stellar enhancement to practical PtM nanoparticle (NP) electrocatalysts with electronic and structural profiles mimicking the SC $Pt_3Ni(111)$,[14,15] however, have been largely unsuccessful. This arises in part due to difficulties in translating a close congruence of the structural and electronic properties of PtM NPs under *in situ* operating conditions with model systems. Current efforts primarily involve an experimental approach that varies the precursors and preparation conditions to maximize performance, but often without total characterization of the particle structure and surface morphology.

Substantial progress has been made in characterizing PtM NPs, albeit under *ex situ* conditions, by employing advanced electron microscopy and other spectroscopic techniques.[13−15] Using *ex situ* scanning transmission electron microscopy (STEM), a "sandwich-segregation" structure, analogous to the layered structure in $Pt_3Ni(111)$,[9] was recently identified in some Pt_3Co NPs.[16] The notably higher ORR specific activity (SA) of these NP's was attributed to the abundant subsurface Co.[16] However, Xin et al.[17] reported that the near subsurface Co of similar heat-treated Pt_3Co NPs does not sustain exposure to acid, and therefore the catalytic enhancement was attributed to strain effects from the deeper Co, instead of the nearest-neighbor electronic effects. Later, Cui et al.[15] reported that, among three different octahedral Pt_xNi_{1-x} NP catalysts, Pt_1Ni_1 exhibited the highest ORR activity owing to the enriched subsurface Ni in the Pt(111) facets. The importance of ordering within the PtM core is also not clear. Wang et al.[18] claimed that Pt_3Co NPs with ordered cores exhibit higher activity and stability than those with disordered cores. However, this disagrees with previously reported results showing the opposite effect.[19] These contradictory reports arise in part from the limitations of *ex situ* characterization, since the near-surface composition and core ordering of PtM NPs often change during electrochemical potential cycling.[15,20]

Received: July 18, 2014
Revised: August 18, 2014
Published: August 19, 2014

dx.doi.org/10.1021/jp507204k | *J. Phys. Chem. C* 2014, 118, 20496−20503

It is essential to obtain atomic-scale structural information on PtM NPs under ORR operating conditions.

Herein, we address this challenge by characterizing the bulk and near-surface structures of a dealloyed Pt_1Co_1/C NP catalyst under ORR conditions using *in situ* X-ray absorption spectroscopy (XAS) in conjunction with multiple-scattering EXAFS (extended X-ray absorption spectroscopy) fitting and surface-sensitive $\Delta\mu$-XANES[21−23] (X-ray absorption near-edge structure) analysis. This offers a unique opportunity to directly correlate the enhanced ORR activity of the catalyst to its atomic structure and morphology by performing *ab initio* real-space FEFF8[24] calculations, based on the structural models arrived at with experimental input. These novel approaches are applicable to a broad range of bimetallic NP catalysts and can lead to a fundamental understanding of the correlation between structure and catalytic properties.

EXPERIMENTAL SECTION

Catalyst Preparation. The dealloyed Pt_1Co_1/HSC was produced via a three step process: (1) the precursor was prepared by an impregnation method, (2) followed by a high temperature annealing step, and (3) chemically dealloyed by acid leaching as described in ref 25. The final catalyst powder was then manually ground in an agate mortar and pestle prior to preparing the MEA inks.

Cell Assembly. The MEAs were fabricated by a standard catalyst-coated membrane (CCM) method via draw down with a Meyer rod and subsequent decal transfer. This information is described elsewhere.[4]

MEA Tests. The above-prepared 50 cm^2 MEAs were tested for their cathode ORR kinetic activities under H_2/O_2 (anode/cathode); H_2/O_2 stoichiometries of 2.0 and 9.5, 100% relative humidity, cell temperature of 80 °C, and at a back-pressure of 150 kPa_{abs}. In voltage cycling tests, 200 sccm H_2 into anode and 50 sccm N_2 into cathode were admitted at 150 kPa_{abs}. The cell voltage was swept at 50 mV s^{-1} between 0.6 and 1.0 V (RHE) in a triangle profile for up to 30 000 cycles. The MEAs were subjected to the cathode catalytic activity (H_2/O_2) and the H_2/air performance tests at 0, 10 000, and 30 000 cycles of voltage cycling. Data collection procedures and conditions, specifically the ORR ECSA measurements, were performed according to the guidelines set by the USCAR Fuel Cell Tech Team (http://www.uscar.org/guest/view_team.php?teams_id=17).

Electrode Preparation and XAFS Data Collection. The electrode inks for the EXAFS electrodes were composed of 1:1 (wt %) 18.2 MΩ purity deionized water (Millipore) and 2-propanol (HPLC-grade, Aldrich), a 5 wt % Nafion solution (Aldrich), and the catalyst powder. The composition was chosen to give a final electrode with a dry Nafion loading of 5 wt %. The ink was hand-painted onto a Zoltek carbon cloth and dried for 15 min in a 65 °C vacuum oven between coats. The final Pt and Co geometric loadings were chosen to give 0.1 edge heights at the Pt L_3 and Co K edges, respectively. All data were collected in the fluorescence mode via a PIPS detector (Canberra) at beamline XOR-9BM at the Advanced Photon Source (Argonne National Lab, Argonne, IL). All of the experimental data were collected in conjunction with the appropriate reference foils to aid in energy alignment and normalization. A flow-through cell with continuously pumped 0.1 M $HClO_4$ (GFS Chemicals) was constantly sparged with either argon or oxygen gases (both high purity). A high-purity, multiply wound Au wire (+99.95%, Alfa Aesar) was used as the counter electrode, and a sealed saturated Ag/AgCl electrode (measured −0.283 V vs dynamic hydrogen electrode, BAS) served as the reference electrode. Potentiostatic control was maintained with an Autolab PGSTAT302N potentiostat/galvanostat (MetroOhm/Brinkmann). The voltage cycling limits were 0.05−1.0 V vs RHE. Data collection was performed at the chosen potentials held during anodic sweeps. Before each measurement, the cell was held for at least 5 min to reach a pseudosteady state (Figure S1). The electrode was fully cycled following each potential hold in order to clean the electrocatalyst surfaces after each potential hold.

High Angle Annular Dark Field Scanning Transmission Electron Microscopy (HAADF STEM). HAADF STEM imaging was performed on the dealloyed Pt_1Co_1/C catalyst NPs with an aberration-corrected JEOL JEM-2100F microscope in a scanning transmission electron microscopy (STEM) mode operated at 200 kV. Samples suitable for the HAADF imaging were prepared by grinding the as-synthesized powder between two clean glass slides and then dusting the ground fine powder onto lacy-carbon-coated Cu TEM grids.

RESULTS AND DISCUSSION

A dealloyed Pt_1Co_1/C catalyst (with a post-dealloying composition of $Pt_{2.2}Co$ as quantified by inductively coupled plasma (ICP) measurements) was prepared via an impregnation method followed by a chemical dealloying step in nitric acid.[25] 50 cm^2 geometric area MEA tests (0.2 mg_{Pt} cm^{-2} loading) in O_2/H_2 revealed an initial Pt-based mass activity (MA) at 0.9 V vs RHE of 0.49 A mg_{Pt}^{-1} (Figure 1),[26] exceeding the 2017 DOE target of 0.44 A mg_{Pt}^{-1}.[27] The MA declined to only 0.32 A mg_{Pt}^{-1} after 30 000 voltage cycles (0.6−1.0 V vs RHE), thereby also meeting the 2017 DOE durability targets.[27]

HAADF STEM imaging (Figure 2) revealed that the as-synthesized catalyst had ∼90% of the particles within the 3−5 nm size range, and each particle showed an alternating arrangement of individual layers of atoms of different intensities. In the HAADF imaging, the image intensity is a function of mass (or thickness) and atomic number Z (proportional to $Z^{\sim 1.7}$).[28] The intensity of the Pt atoms (atomic number 78) will be about 6 times higher than that of the Co atoms (atomic number is 27). For a small PtCo nanoparticle (3−5 nm), the difference in the thickness from the particle center to the outer region is very small, almost negligible. Therefore, the HAADF image in Figure 2a shows alternating bright (due to Pt) and dark (due to Co) layers with ordered Pt and Co atomic planes seen along the electron beam direction in Figure 2b which is probably along the [100] zone axis of the ordered Pt_1Co_1 structure ($P4/mmm$, $L1_0$). A profile of a line scan in Figure 2c shows the intensities of alternating Pt and Co atomic planes. Similar observations of alternating Pt and Co atomic planes were made in ordered Pt_3Co_1 structure ($Pm3m$, $L1_2$).[16,18] On the other hand, the disordered $PtCo_3/C$ NPs undergoing the same dealloying and preparation process as that of the Pt_1Co_1/C NPs do not contain alternating Pt and Co atomic planes as revealed by HAADF.[25] This gives direct evidence of nonrandom Pt and Co distributions, which arises exclusively from ordered PtCo structures.[16−18]

To elucidate whether the ordered structure is sustained during the ORR in 0.1 M $HClO_4$, *in situ* XAS experiments were carried out with a specially designed electrochemical XAS half-cell.[29] The XAS data were processed and analyzed using the IFEFFIT-based Athena and Artemis programs.[30] Striking differences in XANES and Fourier-transformed (FT) EXAFS data between the dry electrode and the electrode under *in situ*

dx.doi.org/10.1021/jp507204k | J. Phys. Chem. C 2014, 118, 20496−20503

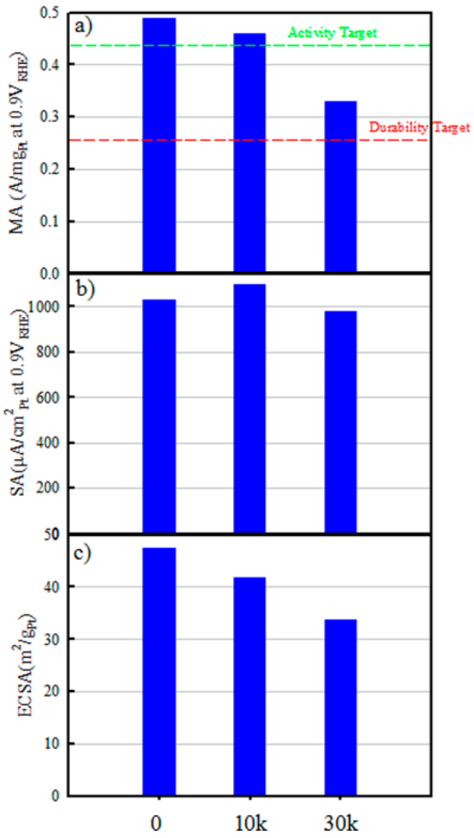

Figure 1. (a) Mass activity, (b) electrochemical surface area, and (c) specific activity of the dealloyed Pt_1Co_1/C catalyst during the voltage cycling tests of MEAs. Conditions: 80 °C, 100% RH, 50 sccm H_2 in anode, 200 sccm N_2 in cathode, voltage range of 0.6−1.0 V (vs RHE), and scan rate at 50 mV s^{-1}. The 2017 DOE target of mass activity and durability are indicated as green and red dashed line, respectively.

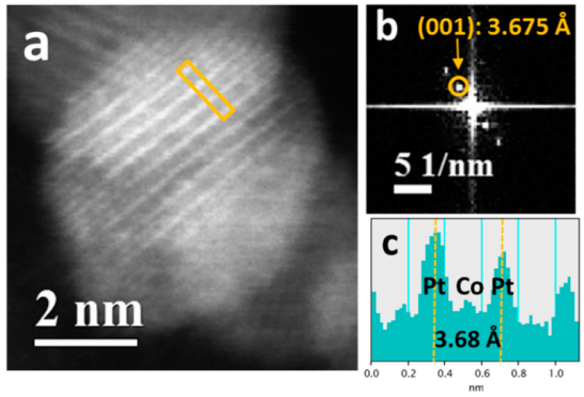

Figure 2. (a) A typical HAADF image of (as-synthesized) dealloyed Pt_1Co_1/C NPs showing an ordered structure with alternating Pt−Co atomic planes. (b) Diffractogram showing the (100) atomic planes, in which case the electron beam was probably oriented to the [100] zone axis of the fct-structured Pt_1Co_1 phase ($P4/mmm$, $L1_0$) as suggested by the interspacing of two bright planes (3.68 Å). This phase is also confirmed by EXAFS as shown later. Based on the ordered Pt_1Co_1 $L1_0$ structural model and the difference in the image intensity of Pt and Co atoms, the bright and dark atomic planes in the HAADF image in (a) probably consist of Pt (100%) atoms and Co (100%) atoms, respectively. (c) A line profile obtained from the region (1.3 × 0.4 nm window highlighted by the yellow rectangle in (a)) showing the intensities of the alternating bright (Pt) and dark (Co) atomic planes. The interspacing of two bright planes is 3.68 Å, corresponding to the (001) plane of the fct-structured $L1_0$ Pt_1Co_1 phase.

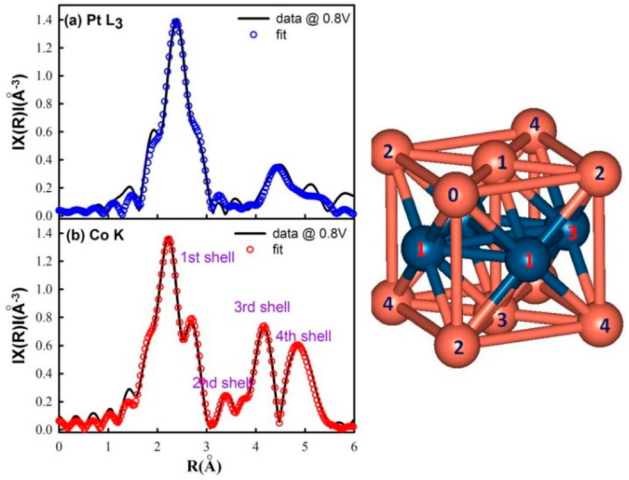

Figure 3. Fourier-transformed EXAFS data (solid line) at Pt L_3 edge (top) and Co K edge (bottom) collected from dealloyed Pt_1Co_1/C at 0.8 V in 0.1 M $HClO_4$ and the full SS+MS fits (circles). The cluster is the unit cell of the Pt_1Co_1 structure ($P4/mmm$, $L1_0$) that was used for the fits. Orange and blue balls represent Co and Pt, respectively. The ball labeled "0" indicates the absorbing Co atom, and the balls labeled "n" represent the atoms in the nth shell.

electrochemical control are clearly shown in Figure S2, indicating their dissimilar electronic and structural properties. This highlights the necessity of characterizing the electrodes under *in situ operando* conditions. The Pt L_3 and Co K edge spectra collected at various potentials in N_2-sparged 0.1 M $HClO_4$ are provided in Figure S3.

A full analysis of the EXAFS data involves analyzing the Pt L_3 edge, involving Pt−Pt and Pt−M scattering, and the M K-edge, involving M−M and M−Pt scattering. Further, both single-scattering (SS) and multiple-scattering (MS) paths can provide significantly more structural information on the NP structure (such as the shape, size, and morphology) than a typical first shell SS path analysis.[31,32] A full EXAFS analysis has rarely been performed on PtM NPs as their lack of long-range order and heterogeneous nature make the multiple scattering fitting arduous. However, as shown by the Co K edge Fourier-transformed (FT) EXAFS data in Figure 3, the dealloyed Pt_1Co_1/C NPs yielded distinctively large signals at relatively large R; these arising from both SS paths to higher shells and MS paths. Inspired by these prominent higher-shell peaks, we carried out a full SS + MS path analysis of both the Pt L_3 and Co K edge EXAFS data up to the fourth shell. The higher-shell fitting analysis can be greatly simplified due to the limited number of MS paths contributing to the largest amplitude in the close-packed structures, allowing the other paths to be neglected.[31−33] In this case, the long-range interactions were approximated by using only the single-scattering paths (SS) and the collinear double- (DS) and triple- (TS) scattering paths (when the scattering angles are equal to 0° or 180°)[31] that were found to be important in the fits to the reference foil data. The two noncollinear triangular paths were found to be significant in fitting the foils but not in fitting the samples.

The measured Pt L_3 and Co K edge data were first fitted individually using a disordered face-centered cubic (fcc) PtCo ($Fm3m$ 225, A1) structural model. At each edge, the energy shift (ΔE) for all the paths was fixed to be the same. At the Co K edge we noticed that some paths, which theoretically do not

dx.doi.org/10.1021/jp507204k | J. Phys. Chem. C 2014, 118, 20496−20503

Table 1. Metal−Bond Distances (R) and Coordination Numbers (CNs) Obtained by Simultaneously Fitting the Pt L_3 and Co K Edge Data Collected from the Dealloyed Pt_1Co_1/C in N_2 Sparged 0.1 M $HClO_4$ at 0.8 V vs RHE[a]

	1st shell		2nd shell		3rd shell		4th shell	
path	R	CN	R	CN	R	CN	R	CN
Co−Co	2.65(1)	2.3(0.7)	3.74(1)	1.7(1.2)	4.58(1)	2.7(1.6)	5.29(1)	2.9(6.0)
Co−Pt	2.66(1)	8.1(1.0)		(0)[b]	4.61(1)	5.7(4.0)		(0)[b]
Co−Pt−Co (DS)							5.31(1)	2 × 5.2(1.7)[c]
Co−Pt−Co−Pt (TS)							5.31(1)	5.2(1.7)[c]
Pt−Pt	2.70(1)	5.1(1.1)		0	4.72(1)	6.5(2.2)	5.40(1)	6.2(3.1)
Pt−Co	2.66(1)	2.9(0.6)		(0)[b]	4.61(1)	2.2(3.1)	5.29(1)	0
Pt−Pt−Pt (DS)							5.40(1)	2 × 1.4(2.4)[c]
Pt−Pt−Pt−Pt (TS)							5.40(1)	1.4(2.4)[c]

[a]Fitting was performed in R-space, $k^{1,2,3}$ weighting. The amplitude reduction factors for the Pt L_3 and Co K edges were determined to be 0.8 and 0.76, respectively, using the full SS+MS fitting on the corresponding Pt and Co reference foil separately following the approach developed by Frenkel.[31] For Pt, $1 < R < 5.5$ Å and $\Delta k = 2.71-12.26$ Å^{-1} were used; for Co, $1 < R < 5.53$ Å and $\Delta k = 2.62-11.59$ Å^{-1} were used. [b](0) indicates that no such path exists in the Pt_1Co_1 $L1_0$ structure. [c]The relationships between the CNs of the two paths in the model are used as constraints for fitting. The ΔE values of the Co K and Pt L_3 edges were -3.6 ± 0.5 and 6.5 ± 0.8 eV, respectively. The R-factor values of the Co K edge and L_3 edge fits were 0.01 and 0.02, respectively. Debye−Waller factors (DWFs) determined for each path are given in Table S1.

exist in certain ordered structures, were associated with a very small coordination number or could not be determined by the fitting. Better fitting results were obtained without including these paths in the fits. Based on this observation, high quality SS + MS fittings were acquired by adopting an ordered face-centered tetragonal (fct) Pt_1Co_1 structural model ($P4/mmm$, 123, $L1_0$). In addition, we noticed that the higher-shell SS Co−Co bond distances (Table 1) are highly consistent with the extension of the first-shell model. Therefore, the change in half-path length (ΔR) for all these paths were assigned as alpha*reff to reduce the variables. Here alpha is the isotropic lattice expansion, and reff is the theoretical length of the current path. The same setting was also used for all the higher-shell SS Co−Pt paths. For DS and TS paths, only the paths with the alternative arrangement of Pt and Co (Table 1) were found significant and thus included in the fit, indicating the nonrandom distribution of Pt and Co atoms. The DS and TS paths were constrained to share the same ΔR and bond length disorder σ^2, which were allowed to vary independently. The correlation between their CNs was constrained as $CN_{DS} = 2CN_{TS}$ according to the theoretical model. The $\sigma^2(s)$ were varied independently for all of the other paths.

Similar settings and constraints were used for the fitting of the Pt L_3 edge data except as follows. First, we found that either ordered or disordered models could fit the Pt L_3 edge data well. Second, no constraints between the SS Pt−Pt bond lengths were adopted since such a relationship was not observed in the fitting of the Pt L_3 edge data, implicating the lack of long-range order and random substitution of atoms of different types.[31] Accordingly, for DS and TS paths, only the paths without the alternative arrangement of Pt and Co (Table 1) were found significant and included in the fit. Third, all the paths, which included only Pt atoms, were assigned to one σ^2, and the paths, which included both Pt and Co atoms, were assigned a different σ^2. The measured Pt L_3 and Co K edge data were then fitted simultaneously using the ordered structural model with further constraints as following: $R_{Pt-Co} = R_{Co-Pt}$ and $\sigma^2_{Pt-Co} = \sigma^2_{Co-Pt}$, which are the bond distance and disorder of the Pt−Co (or Co−Pt) scattering paths, respectively.

The MS paths are fit with remarkably high quality, especially at the Co K edge, using an ordered Pt_1Co_1 structural model ($P4/mmm$, $L1_0$) as seen in Figure 3. The first shell coordination numbers (CNs) to Co (Table 1) are close to those of the Pt_1Co_1 $L1_0$ (bulk) model within the fitting uncertainties. The ratio of the Co−Pt to Co−Co CNs (0.47) in the third shell is also consistent with that of the Pt_1Co_1 $L1_0$ model (0.5). Most importantly, the large CNs for the Co−Pt collinear double- (DS) and triple- (TS) scattering paths (when the scattering angles are equal to 0° or 180°)[31] establish the alternating arrangement of Pt and Co atoms. Such an alternating arrangement belongs exclusively to the PtCo ordered structures like $L1_0$ or $L1_2$.[34] The apparent "expected" environment of Co out to the fourth shell, quantitatively determined by the full SS +MS path analysis, rules out the possibility of disordered structures. Note that the Co K edge data were collected *in situ* at 0.8 V vs RHE while immersed in an aggressively oxidizing environment of 0.1 M perchloric acid under which metallic Co cannot survive. The Co atoms are located only in the core of the dealloyed Pt_1Co_1 NPs, which is directly supported by the larger first shell CN for Co than that for Pt (Table 1). Thus, the full SS+MS fitting gives strong evidence for an ordered Pt_1Co_1 $L1_0$ core. This is the first instance, that we are aware, where the ordered nature of a PtM NP core, after exposure to an electrochemical environment under ORR conditions, has been established by an *in situ* full SS+MS path EXAFS analysis.

In contrast to the FT and fit quality at the Co K edge, the higher-shell structure at the Pt L_3 edge (Figure 3, top) is not as intense, and the MS fit quality is relatively modest. Although the Pt_1Co_1 $L1_0$ structure was adopted for the structural model as indicated above, we found that an ordered Pt_3Co_1 model ($Pm3m$, $L1_2$) or even a disordered PtCo ($Fm3m$, A1) model can fit the Pt L_3 EXAFS data without significant compromise in quality, whereas only the Pt_1Co_1 model ($P4/mmm$, $L1_0$) can fit the Co K edge data well. At higher shells, Pt is coordinated more to Pt than Co, contrasting the environment found at the Co K edge where Co−Pt interactions are present in higher shells. These results indicate the local coordination environment of Pt cannot be exclusively assigned to ordered PtCo structures. Unlike Co that locates exclusively in the Pt_1Co_1 core, the Pt in the NPs locate in the Pt_1Co_1 core as well as the surface, which is supported by the smaller first shell coordination number of Pt compared to that of Co (Table 1) since atoms on surfaces are undercoordinated. Apparently, the local coordination environment of the Pt in the core is quite different from that of the Pt on the surface. Note that the Pt L_3 EXAFS data are averaged over all the Pt atoms in the NPs and

dx.doi.org/10.1021/jp507204k | J. Phys. Chem. C 2014, 118, 20496−20503

thus cannot be well fitted with one specific model. Since the Pt atoms embedded in the ordered Pt_1Co_1 $L1_0$ core must have the same long-range order exhibited by the alternating arrangement of Pt or Co atoms, these results indicate that excess Pt atoms located near the outer surface of the NPs are in a disordered structure.

The averaged bond distances determined by EXAFS analysis are given in Table 1. The higher-shell Co−Co single scattering (SS) bond distances are highly consistent with the extension of the first-shell structure, further confirming the periodic long-range order structure seen by Co. The averaged first shell Co−Pt and Co−Co bond distances are 2.66 and 2.65 Å, respectively. These are comparable to those in a bulk Pt_1Co_1 $L1_0$ structure (a = 3.79 Å, c = 3.68 Å) identified here and elsewhere,[35] 2.64 Å, and 2.68 Å, respectively. Compared to other extensively studied Pt_3Co NPs, the higher content of Co in the Pt_1Co_1 cores leads to a smaller lattice constant as expected from Vegard's law. Moreover, an ordered $L1_0$ Pt_1Co_1 core has a much smaller "c" lattice parameter (3.68 Å) than that of a disordered A1 Pt_1Co_1 one (3.835 Å). Consequently, the bulk Pt−Pt bond distance (2.70 Å) in dealloyed Pt_1Co_1 NPs is shorter than that reported in various PtCo alloys,[4,36,37] producing the stronger compressive strain that is widely acknowledged as the dominant effect enhancing the ORR activity of dealloyed PtM catalysts.[38]

Another advantageous feature of the ordered Pt_1Co_1 $L1_0$ structure is the Co-enriched subsurface. Previous studies have confirmed that the subsurface Co content in ordered Pt−Co NPs is higher than that in disordered Pt−Co NPs.[16,19] Notably, the (100) facet of the ordered Pt_1Co_1 $L1_0$ phase exhibits the desired "sandwich-segregation" structure with the segregation of Pt to the surface and segregation of Co to the subsurface.[16,34] The ordered PtM (such as PtPd[39]) with an onion-ring structure can even exhibit the "sandwich-segregation" structure at the (111), (110), and (100) facets owing to its unique shell-by-shell alternating arrangement of Pt or M. The resultant compositional profiles in the near-surface region of the ordered Pt−Co NPs are analogous to those of polycrystalline Pt_3M with Pt-skin surfaces[13] or the SC $Pt_3Ni(111)$.[9] It is thus of particular interest to explore whether the subsurface Co can remain in an acidic environment and not dealloy. The XAS characterization conducted under *in situ* reactive conditions offers us good opportunilities to address this question.

The particle size, bulk composition, and atomic distribution of the NPs; properties which are the most relevant for determining the critical morphology of bimetallic NPs can be quantitatively determined by the full SS+MS fittings. The averaged first shell CN of the dealloyed Pt_1Co_1 NPs is 8.8 ± 1.7. Accordingly, the averaged particle size is estimated to be in the range of 2−5 nm,[40] consistent with the HAADF STEM results in spite of the large uncertainties. Meanwhile, the bulk composition $n_{Pt/Co}$ is determined to be 2.8 ± 0.7 using the following correlation:[41,42] $n_{Pt/Co} = CN_{Co-Pt}/CN_{Pt-Co}$. This result is close to that obtained by ICP (2.2). In addition, the J_{Pt} and J_{Co} order parameters,[43] which can be used to quantitatively characterize the atomic distribution or alloying extent of bimetallic NPs, are determined to be 1.34 and 1.06, respectively. Both are higher than those expected for perfectly alloyed (i.e., disordered) NPs (J_{Pt} = J_{Co} = 1), indicating the nonrandom distribution of the Pt and Co atoms. These results show the self-consistency of the different experimental techniques used in this work and validate the particle size, bulk composition, and atomic distribution of the NPs indicated here.

In modeling these data, the best agreement with all the experimental results is accomplished when one atomic layer of Pt is placed in an outer shell on a cuboctahedron PtCo $L1_0$ cluster with 309 atoms (a magic number) distributed in 4 ALs, corresponding to a 3 nm diameter NP with a $PtCo_{core}$−Pt_{shell} structure (Figure 4 and Table 2). Note that the alternating arrangement of individual layers of atoms revealed in the HAADF STEM images (Figure 2) is reproduced by the model. Similarly, for a 5 nm Pt@PtCo NP, a ∼1.5 AL Pt shell enclosing a PtCo $L1_0$ core provides the best match to the experimental data. Giving a particle size range of 3−5 nm, the models predict a nontrivial number of Co atoms in the immediate subsurface of the dealloyed Pt_1Co_1 NPs.

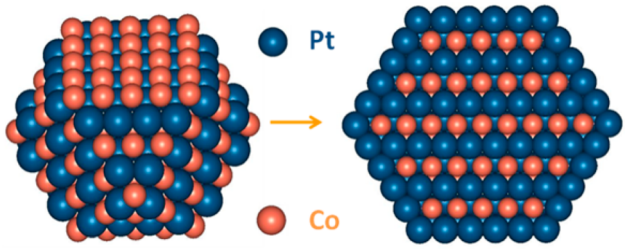

Figure 4. A $Co_{165}Pt_{144}$ cuboctahedron cluster with $L1_0$ structure (left: perspective 3D view) covered with one Pt atomic layer gives a Pt_{252}@$Co_{165}Pt_{144}$ ordered core−shell cluster model (right: cross-section view).

Table 2. Quantitative Structural Properties Obtained by the EXAFS Experimental Full SS+MS Fitting and Calculated from the Pt@PtCo NP Model

	CN_{avg}[a]	$n_{Pt/Co}$	J_{Pt}	J_{Co}
EXAFS	9.0 ± 1.9	2.8 ± 0.7 (ICP: 2.2)	1.34	1.06
model	10	2.4	1.35	1.04

[a]The averaged first-shell CN of the dealloyed Pt_1Co_1 NPs, which can be used to identify the average particle size of small NPs (<5 nm). $n_{Pt/Co}$ is the atomic ratio. J_{Pt} and J_{Co} quantitatively determine the atomic distribution of the NPs. As seen, these four quantities, which are the most relevant properties for the analysis of the morphology of bimetallic NPs, can be simultaneously reproduced closely by the NP model (as shown in Figure 4, right). In addition, the onion-type (shell-wise) alternating arrangement of Pt or Co as shown Figure 2 is clearly seen here.

The near-surface composition was further explored with the surface sensitive $\Delta\mu = \mu(V) - \mu(V_{ref})$ XANES technique.[21−23] This method, essentially a XANES difference technique, cancels out the large scattering signals from the unreactive bulk, thereby isolating the effects of adsorbates (e.g., OH*, O*, etc.) on the Co XANES spectra. Figure 5 presents Co K edge $\Delta\mu$ signatures at four different potentials in N_2-sparged 0.1 M $HClO_4$. (The normalized Co K edge XANES spectra are provided in Figure S3.) The 0.54 V signal (N_2) was used as the reference as little to no direct absorption of oxygen species is expected at this double layer potential. Comparisons with previous Co $\Delta\mu$ studies[44] reveal that the signals show markedly different signatures and cannot be explained by direct OH* adsorption onto Co. Subsequent Co K-edge FEFF8[24] calculations performed on a six-atom Janin-type cluster[45] reveal that the $\Delta\mu$ signature at 0.7 V is reproduced by placing an O atom at the atop (one-fold) position of a Pt atom adjacent to

dx.doi.org/10.1021/jp507204k | J. Phys. Chem. C 2014, 118, 20496−20503

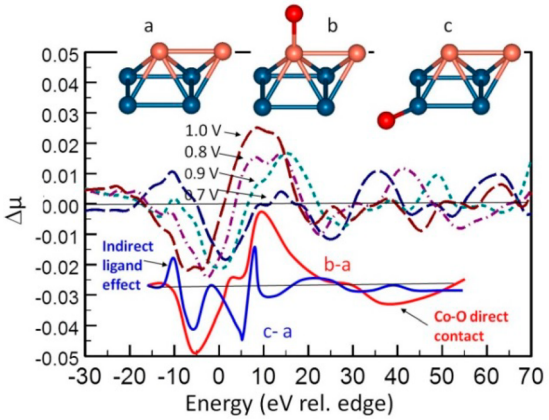

Figure 5. Comparison of the Co K edge $\Delta\mu = \mu(V) - \mu(0.54\ V)$ for a dealloyed Pt_1Co_1 in N_2-sparged 0.1 M $HClO_4$ at the indicated potentials (V vs RHE). Top: Pt_4Co_2 Janin clusters utilized in the FEFF8 calculations (blue = Pt, orange = Co, red = O). Middle: experimental Co K edge $\Delta\mu$ curves at the indicated potentials. Bottom: theoretical FEFF8 calculated $\Delta\mu$ curves derived from the shown models.

the absorbing Co atom (Figure 3c): $\Delta\mu_{theory} = \mu(O{-}Pt_4Co_2) - \mu(Pt_4Co_2)$. The $\Delta\mu$ spectra calculated based on a bigger $Pt_{16}Co_9$ cluster produced results that are essentially the same as those calculated on the six-atom cluster (Figure S4).

While the Co K edge $\Delta\mu$ signature at 0.7 V is indicative of an oxygen atom adsorbed on Pt above the Co, the signature at 1.0 V matches more closely the theoretical $\Delta\mu$ curve obtained from an O atom directly bound to Co (Figure 5b). As illustrated in Scheme 1, at low potentials, Co in the subsurface is well

Scheme 1. Cross Sections of the Dealloyed Pt_1Co_1/C Catalyst[a]

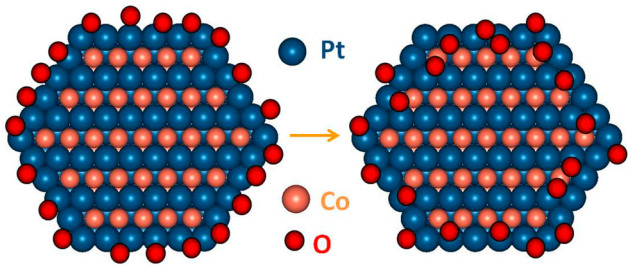

[a]At 0.7 V, adsorbed O is found only on the Pt surface (left), and the Co K edge $\Delta\mu$ signals arise from electronic or ligand effects; at 1.0 V, O place exchange with Pt results in direct Co−O interactions.

protected by an outer layer of (surface) Pt from O(H), and the $\Delta\mu$ signature arises from ligand/electronic effects on the subsurface Co caused by the O(H) adsorption on the surface Pt. At higher potentials, place exchange between Pt and O occurs[46] and enables O to penetrate below the Pt surface resulting in direct Co−O bonding. Thus, the presence of a nontrivial amount of Co in the immediate subsurface atomic layer of the particle is suggested, consistent with the modeling results.

The confirmation of the subsurface Co atoms in the ordered Pt_1Co_1 NPs under harsh acidic *in situ* conditions strongly suggests that these Co atoms are well protected by the nonporous Pt-dominated surface, since exposed Co is normally highly soluble in acid. This is further suggested by the different behaviors we have found with different $PtCo_n$ precursors. Beginning with the Pt_1Co_1 precursor characterized above, results in $Pt_1Co_{0.45}$ while beginning with a Pt_1Co_3 precursor results in $Pt_1Co_{0.37}$[25] undergoing the same dealloying and preparation process: a ∼54% loss of Co in the former compared to ∼88% in the latter. Accordingly, the majority of NPs in the dealloyed Pt_1Co_3 show a thicker porous Pt shell surrounding multiple-disordered PtCo cores—very different from the structure of the dealloyed Pt_1Co_1 structure identified here (an ultrathin but nonporous Pt shell surrounding an ordered PtCo core). These results are consistent with previous findings,[47,48] namely, that the depletion of the soluble transition metal M in PtM_x alloys with low M concentration ($x \leq 1$) in acidic pH environment is limited to the surface region, resulting in a thin Pt-rich shell and a single M-rich core structure. In contrast, the M retreats into the inner cores of PtM_x NPs with high M concentration ($x \geq 1$), leading to a thick porous Pt-rich shell with multiple M-rich cores (also referred to as a porous disordered core). The single core−nonporous shell structure of the ordered Pt_1Co_1 NPs protects the subsurface Co against dealloying and likely accounts for the high NP stability as suggested by Strasser et al.'s recent work.[49] Therefore, the compositional profiles of the Pt_1Co_1 NPs are sustained in acid, as the subsurface Co is stabilized by the ordered Pt_1Co_1 core and well protected by the integral nonporous Pt overlayer. This makes the ordered PtCo core−ultrathin Pt shell NP structure promising as an ORR catalyst, as it possesses electronic and atomic profiles that mimic the SC $Pt_3Ni(111)$[9] or other extended Pt-skin surfaces of much larger polycrystalline Pt_3M materials.[13]

Following the confirmation of an atomically ordered core−nonporous shell structure enables *ab initio* theoretical electronic structure calculations (such as with the FEFF8 code) on well-defined experimentally determined structural models, to determine the influences of the electronic properties. Only the (111) and (100) facets are compared in calculations as they represent the predominate surfaces on small metallic NPs. In a previous study[12] we reported that the d-band centers (ε_d) of a $Pt_{19}Co_6(111)$ cluster with a "sandwich" structure (Figure S4) and a pure $Pt_{25}(111)$ surface were equal to −3.30 and −3.03 eV, respectively. Similarly, the calculated ε_d for $Pt_{10}Co_4(100)$ and pure $Pt_{14}(100)$ clusters (Figure S5) are −2.74 and −2.58 eV, respectively. Although these calculated values of the d-band center are still virtual as the surface R_{Pt-Pt} in $Pt@Pt_1Co_1$ NPs deviates slightly from the bulk average R_{Pt-Pt} given by EXAFS owing to the surface relaxation,[38] the calculations clearly show that on both planes the ε_d is significantly shifted by the presence of Co. Thus, the high specific activity of the dealloyed Pt_1Co_1/C catalyst can be largely attributed to its unique morphology, with Co enrichment in the ordered core and at the subsurface—both promoting the downshift of ε_d by way of cooperative compressive-strain and surface ligand effects.

■ CONCLUSIONS

In conclusion, we presented both experimental and theoretical results on a novel dealloyed Pt_1Co_1 NP catalyst with Pt mass activity ∼4 times higher than those of Pt/C and with superior stability in PEMFCs. This catalyst possesses a unique ordered PtCo core−ultrathin with nonporous Pt shell structure as shown by *ex situ* HAADF-STEM and *in situ* XAS techniques. This structure maintains the desired compositional profiles in the near-surface region even during the ORR in acid, as the subsurface Co is enriched by the ordered Pt_1Co_1 core and well

dx.doi.org/10.1021/jp507204k | J. Phys. Chem. C 2014, 118, 20496−20503

protected by the integral nonporous Pt overlayer. *Ab initio* FEFF8 calculations reveal that the enhanced activity can be attributed to cooperative compressive-strain and ligand effects induced by the Co enrichment in the compact core and near subsurface. The novel experimental methodology used in this work to characterize the atomic structures of these materials under reaction conditions will likely encourage the rational design and synthesis of other bimetallic catalysts.

■ ASSOCIATED CONTENT

Supporting Information

Additional information including the XAS spectra at the Pt L_3 and Co K edges and the structural models employed for $\Delta\mu$ modeling and FEFF calculations. This material is available free of charge via the Internet at http://pubs.acs.org.

■ AUTHOR INFORMATION

Corresponding Author

*E-mail s.mukerjee@neu.edu; Ph (617)373-2382 (S.M.).

Notes

The authors declare no competing financial interest.

■ ACKNOWLEDGMENTS

This research was supported by the Fuel Cell Technology Program of the Office of Energy Efficiency and Renewable Energy of the U.S. Department of Energy under Contract DE-EE0000458. Use of the Photon Source (beamline XOR-9BM), Argonne National Laboratory, was supported by the U.S. Department of Energy, Office of Science, Office of Basic Energy Sciences, under Contract DE-AC02-98CH10886.

■ REFERENCES

(1) Mukerjee, S.; Srinivasan, S.; Soriaga, M. P.; McBreen, J. Effect of Preparation Conditions of Pt Alloys on Their Electronic, Structural, and Electrocatalytic Activities for Oxygen Reduction - XRD, XAS, and Electrochemical Studies. *J. Phys. Chem.* **1995**, *99*, 4577−4589.

(2) Mukerjee, S.; Srinivasan, S.; Soriaga, M. P.; McBreen, J. Role of Structural and Electronic Properties of Pt and Pt Alloys on Electrocatalysis of Oxygen Reduction. *J. Electrochem. Soc.* **1995**, *142*, 1409−1422.

(3) Toda, T.; Igarashi, H.; Uchida, H.; Watanabe, M. Enhancement of the Electroreduction of Oxygen on Pt Alloys with Fe, Ni, and Co. *J. Electrochem. Soc.* **1999**, *146*, 3750−3756.

(4) Gasteiger, H. A.; Kocha, S. S.; Sompalli, B.; Wagner, F. T. Activity Benchmarks and Requirements for Pt, Pt-Alloy, and Non-Pt Oxygen Reduction Catalysts for PEMFCs. *Appl. Catal., B* **2005**, *56*, 9−35.

(5) Koh, S.; Strasser, P. Electrocatalysis on Bimetallic Surfaces: Modifying Catalytic Reactivity for Oxygen Reduction by Voltammetric Surface Dealloying. *J. Am. Chem. Soc.* **2007**, *129*, 12624−12625.

(6) Oezaslan, M.; Hasché, F.; Strasser, P. Pt-Based Core−Shell Catalyst Architectures for Oxygen Fuel Cell Electrodes. *J. Phys. Chem. Lett.* **2013**, *4*, 3273−3291.

(7) Debe, M. K. Electrocatalyst Approaches and Challenges for Automotive Fuel Cells. *Nature* **2012**, *486*, 43−51.

(8) Stamenkovic, V.; Mun, B. S.; Mayrhofer, K. J. J.; Ross, P. N.; Markovic, N. M.; Rossmeisl, J.; Greeley, J.; Nørskov, J. K. Changing the Activity of Electrocatalysts for Oxygen Reduction by Tuning the Surface Electronic Structure. *Angew. Chem., Int. Ed.* **2006**, *45*, 2897−2901.

(9) Stamenkovic, V. R.; Fowler, B.; Mun, B. S.; Wang, G.; Ross, P. N.; Lucas, C. A.; Marković, N. M. Improved Oxygen Reduction Activity on $Pt_3Ni(111)$ via Increased Surface Site Availability. *Science* **2007**, *315*, 493−497.

(10) Stamenkovic, V. R.; Mun, B. S.; Mayrhofer, K. J. J.; Ross, P. N.; Markovic, N. M. Effect of Surface Composition on Electronic Structure, Stability, and Electrocatalytic Properties of Pt-Transition Metal Alloys: Pt-Skin versus Pt-Skeleton Surfaces. *J. Am. Chem. Soc.* **2006**, *128*, 8813−8819.

(11) Greeley, J.; Stephens, I. E. L.; Bondarenko, A. S.; Johansson, T. P.; Hansen, H. A.; Jaramillo, T. F.; Rossmeisl, J.; Chorkendorff, I.; Nørskov, J. K. Alloys of Platinum and Early Transition Metals as Oxygen Reduction Electrocatalysts. *Nat. Chem.* **2009**, *1*, 552−556.

(12) Jia, Q.; Segre, C. U.; Ramaker, D.; Caldwell, K.; Trahan, M.; Mukerjee, S. Structure−Property−Activity Correlations of Pt-bimetallic Nanoparticles: A Theoretical Study. *Electrochim. Acta* **2013**, *88*, 604−613.

(13) Stamenkovic, V. R.; Mun, B. S.; Arenz, M.; Mayrhofer, K. J. J.; Lucas, C. A.; Wang, G.; Ross, P. N.; Markovic, N. M. Trends in Electrocatalysis on Extended and Nanoscale Pt-Bimetallic Alloy Surfaces. *Nat. Mater.* **2007**, *6*, 241−247.

(14) Choi, S.-I.; Xie, S.; Shao, M.; Odell, J. H.; Lu, N.; Peng, H.-C.; Protsailo, L.; Guerrero, S.; Park, J.; Xia, X.; et al. Synthesis and Characterization of 9 nm Pt−Ni Octahedra with a Record High Activity of 3.3 A/mg_{Pt} for the Oxygen Reduction Reaction. *Nano Lett.* **2013**, *13*, 3420−3425.

(15) Cui, C.; Gan, L.; Heggen, M.; Rudi, S.; Strasser, P. Compositional Segregation in Shaped Pt Alloy Nanoparticles and their Structural Behaviour during Electrocatalysis. *Nat. Mater.* **2013**, *12*, 765−771.

(16) Chen, S.; Ferreira, P. J.; Sheng, W.; Yabuuchi, N.; Allard, L. F.; Shao-Horn, Y. Enhanced Activity for Oxygen Reduction Reaction on "Pt_3Co" Nanoparticles: Direct Evidence of Percolated and Sandwich-Segregation Structures. *J. Am. Chem. Soc.* **2008**, *130*, 13818−13819.

(17) Xin, H. L.; Mundy, J. A.; Liu, Z.; Cabezas, R.; Hovden, R.; Kourkoutis, L. F.; Zhang, J.; Subramanian, N. P.; Makharia, R.; Wagner, F. T.; et al. Atomic-Resolution Spectroscopic Imaging of Ensembles of Nanocatalyst Particles across the Life of a Fuel Cell. *Nano Lett.* **2011**, *12*, 490−497.

(18) Wang, D.; Xin, H. L.; Hovden, R.; Wang, H.; Yu, Y.; Muller, D. A.; DiSalvo, F. J.; Abruña, H. D. Structurally Ordered Intermetallic Platinum−Cobalt Core−Shell Nanoparticles with Enhanced Activity and Stability as Oxygen Reduction Electrocatalysts. *Nat. Mater.* **2013**, *12*, 81−87.

(19) Watanabe, M.; Tsurumi, K.; Mizukami, T.; Nakamura, T.; Stonehart, P. Activity and Stability of Ordered and Disordered Co-Pt Alloys for Phosphoric Acid Fuel Cells. *J. Electrochem. Soc.* **1994**, *141*, 2659−2668.

(20) Tuaev, X.; Rudi, S.; Petkov, V.; Hoell, A.; Strasser, P. In Situ Study of Atomic Structure Transformations of Pt−Ni Nanoparticle Catalysts during Electrochemical Potential Cycling. *ACS Nano* **2013**, *7*, 5666−5674.

(21) Jia, Q.; Ramaker, D. E.; Ziegelbauer, J. M.; Ramaswamy, N.; Halder, A.; Mukerjee, S. Fundamental Aspects of Ad-metal Dissolution and Contamination in Low and Medium Temperature Fuel Cell Electrocatalysis: A Cu Based Case Study Using in Situ Electrochemical X-ray Absorption Spectroscopy. *J. Phys. Chem. C* **2013**, *117*, 4585−4596.

(22) Teliska, M.; O'Grady, W. E.; Ramaker, D. E. Determination of O and OH Adsorption Sites and Coverage in Situ on Pt Electrodes from Pt L_{23} X-ray Absorption Spectroscopy. *J. Phys. Chem. B* **2005**, *109*, 8076−8084.

(23) Roth, C.; Benker, N.; Buhrmester, T.; Mazurek, M.; Loster, M.; Fuess, H.; Koningsberger, D. C.; Ramaker, D. E. Determination of O[H] and CO Coverage and Adsorption Sites on PtRu Electrodes in an Operating PEM Fuel Cell. *J. Am. Chem. Soc.* **2005**, *127*, 14607−14615.

(24) Ankudinov, A. L.; Ravel, B.; Rehr, J. J.; Conradson, S. D. Real-Space Multiple-Scattering Calculation and Interpretation of X-ray-Absorption Near-Edge Structure. *Phys. Rev. B* **1998**, *58*, 7565−7576.

(25) Yu, Z.; Zhang, J.; Liu, Z.; Ziegelbauer, J. M.; Xin, H.; Dutta, I.; Muller, D. A.; Wagner, F. T. Comparison between Dealloyed $PtCo_3$ and $PtCu_3$ Cathode Catalysts for Proton Exchange Membrane Fuel Cells. *J. Phys. Chem. C* **2012**, *116*, 19877−19885.

(26) Wagner, F. T. In 2012 Annual Merit Review Proceedings - Fuel Cells; U.S. Department of Energy: Hydrogen and Fuel Cells Program: online, 2012; http://www.hydrogen.energy.gov/pdfs/review12/fc087_wagner_2012_o.pdf.
(27) DOE Hydrogen and Fuel Cell Activities, Progress, and Plans, United States Department of Energy, 2009.
(28) Crewe, A. V.; Wall, J.; Langmore, J. Visibility of Single Atoms. *Science* **1970**, *168*, 1338−1340.
(29) Arruda, T. M.; Shyam, B.; Lawton, J. S.; Ramaswamy, N.; Budil, D. E.; Ramaker, D. E.; Mukerjee, S. Fundamental Aspects of Spontaneous Cathodic Deposition of Ru onto Pt/C Electrocatalysts and Membranes under Direct Methanol Fuel Cell Operating Conditions: An in Situ X-ray Absorption Spectroscopy and Electron Spin Resonance Study. *J. Phys. Chem. C* **2009**, *114*, 1028−1040.
(30) Newville, M. IFEFFIT: Interactive XAFS Analysis and FEFF Fitting. *J. Synchrotron Radiat.* **2001**, *8*, 322−324.
(31) Frenkel, A. Solving the Structure of Nanoparticles by Multiple-Scattering EXAFS Analysis. *J. Synchrotron Radiat.* **1999**, *6*, 293−295.
(32) Nashner, M. S.; Frenkel, A. I.; Adler, D. L.; Shapley, J. R.; Nuzzo, R. G. Structural Characterization of Carbon-Supported Platinum−Ruthenium Nanoparticles from the Molecular Cluster Precursor $PtRu_5C(CO)_{16}$. *J. Am. Chem. Soc.* **1997**, *119*, 7760−7771.
(33) Lee, P. A.; Pendry, J. B. Theory of the Extended X-ray Absorption Fine Structure. *Phys. Rev. B* **1975**, *11*, 2795−2811.
(34) Gruner, M. E.; Entel, P. Simulating Functional Magnetic Materials on Supercomputers. *J. Phys.: Condens. Matter* **2009**, *21*, 293201.
(35) Koh, S.; Leisch, J.; Toney, M. F.; Strasser, P. Structure-Activity-Stability Relationships of Pt−Co Alloy Electrocatalysts in Gas-Diffusion Electrode Layers. *J. Phys. Chem. C* **2007**, *111*, 3744−3752.
(36) Chen, S.; Sheng, W.; Yabuuchi, N.; Ferreira, P. J.; Allard, L. F.; Shao-Horn, Y. Origin of Oxygen Reduction Reaction Activity on "Pt_3Co" Nanoparticles: Atomically Resolved Chemical Compositions and Structures. *J. Phys. Chem. C* **2008**, *113*, 1109−1125.
(37) Lai, F.-J.; Sarma, L. S.; Chou, H.-L.; Liu, D.-G.; Hsieh, C.-A.; Lee, J.-F.; Hwang, B.-J. Architecture of Bimetallic Pt_xCo_{1-x} Electrocatalysts for Oxygen Reduction Reaction As Investigated by X-ray Absorption Spectroscopy. *J. Phys. Chem. C* **2009**, *113*, 12674−12681.
(38) Strasser, P.; Koh, S.; Anniyev, T.; Greeley, J.; More, K.; Yu, C.; Liu, Z.; Kaya, S.; Nordlund, D.; Ogasawara, H.; et al. Lattice-Strain Control of the Activity in Dealloyed Core−Shell Fuel Cell Catalysts. *Nat. Chem.* **2010**, *2*, 454−460.
(39) Cheng, D.; Wang, W.; Huang, S. The Onion-Ring Structure for Pd−Pt Bimetallic Clusters. *J. Phys. Chem. B* **2006**, *110*, 16193−16196.
(40) Benfield, R. E. Mean Coordination Numbers and the Non-Metal-Metal Transition in Clusters. *J. Chem. Soc., Faraday Trans.* **1992**, *88*, 1107−1110.
(41) Proffen, T.; Neder, R. B. DISCUS: A Program for Diffuse Scattering and Defect-Structure Simulation. *J. Appl. Crystallogr.* **1997**, *30*, 171−175.
(42) Via, G. H.; Drake, K. F.; Meitzner, G.; Lytle, F. W.; Sinfelt, J. H. Analysis of EXAFS Data on Bimetallic Clusters. *Catal. Lett.* **1990**, *5*, 25−33.
(43) Hwang, B.-J.; Sarma, L. S.; Chen, J.-M.; Chen, C.-H.; Shih, S.-C.; Wang, G.-R.; Liu, D.-G.; Lee, J.-F.; Tang, M.-T. Structural Models and Atomic Distribution of Bimetallic Nanoparticles as Investigated by X-ray Absorption Spectroscopy. *J. Am. Chem. Soc.* **2005**, *127*, 11140−11145.
(44) Teliska, M.; Murthi, V. S.; Mukerjee, S.; Ramaker, D. E. Correlation of Water Activation, Surface Properties, and Oxygen Reduction Reactivity of Supported Pt-M/C Bimetallic Electrocatalysts Using XAS. *J. Electrochem. Soc.* **2005**, *152*, A2159−A2169.
(45) Janin, E.; von Schenck, H.; Göthelid, M.; Karlsson, U. O.; Svensson, M. Bridge-Bonded Atomic Oxygen on Pt(110). *Phys. Rev. B* **2000**, *61*, 13144−13149.
(46) Kongkanand, A.; Ziegelbauer, J. M. Surface Platinum Electro-oxidation in the Presence of Oxygen. *J. Phys. Chem. C* **2012**, *116*, 3684−3693.
(47) Chen, S.; Gasteiger, H. A.; Hayakawa, K.; Tada, T.; Shao-Horn, Y. Platinum-Alloy Cathode Catalyst Degradation in Proton Exchange Membrane Fuel Cells: Nanometer-Scale Compositional and Morphological Changes. *J. Electrochem. Soc.* **2010**, *157*, A82−A97.
(48) Bonakdarpour, A.; Wenzel, J.; Stevens, D. A.; Sheng, S.; Monchesky, T. L.; Löbel, R.; Atanasoski, R. T.; Schmoeckel, A. K.; Vernstrom, G. D.; Debe, M. K.; et al. Studies of Transition Metal Dissolution from Combinatorially Sputtered, Nanostructured $Pt_{1-x}M_x$ (M = Fe, Ni; $0 < x < 1$) Electrocatalysts for PEM Fuel Cells. *J. Electrochem. Soc.* **2005**, *152*, A61−A72.
(49) Gan, L.; Heggen, M.; O'Malley, R.; Theobald, B.; Strasser, P. Understanding and Controlling Nanoporosity Formation for Improving the Stability of Bimetallic Fuel Cell Catalysts. *Nano Lett.* **2013**, *13*, 1131−1138.